ELSEVIER

Journal of Structural Geology 28 (2006) 1468–1482

JOURNAL OF STRUCTURAL GEOLOGY

www.elsevier.com/locate/jsg

Numerical modelling of faulting and fluid flow in porous rocks: An approach based on critical state soil mechanics

H.A. Sheldon [a,*], A.C. Barnicoat [b], A. Ord [a]

[a] *Predictive Mineral Discovery Cooperative Research Centre, CSIRO Exploration and Mining, PO Box 1130, Bentley, WA 6102, Australia*
[b] *Predictive Mineral Discovery Cooperative Research Centre, Geoscience Australia, GPO Box 378, Canberra 2601, Australia*

Received 3 November 2005; received in revised form 30 March 2006; accepted 31 March 2006
Available online 30 June 2006

Abstract

The mechanical behaviour of porous rocks changes from localised, dilatant shear failure to distributed shear-enhanced compaction with increasing porosity, grain size and effective pressure. Shear-enhanced compaction results in permeability reduction, whereas dilatant shear failure results in permeability enhancement if the host rock porosity is low, but reduces permeability if porosity is high. Hence, focused fluid flow requires dilatant shear failure of low porosity rocks. Changes in porosity and effective pressure with depth in sedimentary basins lead to corresponding variations in failure mode and permeability evolution. This study uses results of deformation experiments to parameterise a constitutive behaviour for sandstones, following the principles of critical state soil mechanics. The constitutive behaviour is implemented in a numerical model that couples deformation with permeability evolution and fluid flow. The model is used to investigate effects of grain size, geothermal gradient and deposition rate, verifying previous predictions regarding the relationship between these parameters and the minimum depth at which focused fluid flow may take place. Fluid diverges out of faults or shear zones at the point where they change from fluid pathways to seals. Dilatant faults formed in extension may undergo compaction and strain hardening during basin inversion.

Keywords: Critical state; Cam clay; Sandstone; Fluid flow; Permeability

1. Introduction

Observations of fault rocks from sedimentary basins suggest that some faults act as fluid pathways, while others act as barriers to flow (Knipe, 1992, 1993; Antonellini and Aydin, 1994; Fisher and Knipe, 1998, 2001; Fisher et al., 2003). Faults may act as seals by virtue of their own low permeability, or by juxtaposing low permeability rocks against higher permeability units. Furthermore, faults that act as fluid pathways during and immediately after a deformation event may become impermeable as a result of cementation, thus limiting the amount of fluid that can pass through (e.g. Sibson, 2001; Sheldon and Ord, 2005). This study is concerned with the porosity and pressure-dependence of deformation in porous rocks, the changes in permeability that accompany such deformation, and consequent effects on fluid flow. The effects of cementation, grain size reduction, and clay smears are not considered here, although these processes play an important role in determining the fluid flow characteristics of deformed rocks.

Porous rocks display a transition from dilatant, brittle behaviour to shear-enhanced compaction and macroscopically ductile behaviour with increasing effective pressure. This low-temperature brittle–ductile transition takes place at higher effective pressure with decreasing porosity and grain size (Rutter and Hadizadeh, 1991; Paterson and Wong, 2005). Shear-enhanced compaction always results in significant permeability reduction, whereas dilatant brittle failure may result in increased or decreased permeability, depending

* Corresponding author. CSIRO Exploration and Mining, PO Box 1130, Bentley, WA 6102, Australia. Tel.: +61 8 64368915; fax: +61 8 64368555.
E-mail address: heather.sheldon@csiro.au (H.A. Sheldon).

0191-8141/$ - see front matter © 2006 Elsevier Ltd. All rights reserved.
doi:10.1016/j.jsg.2006.03.039

on the porosity of the undeformed rock (Zhu and Wong, 1997). The variation of porosity and effective pressure with depth in sedimentary basins results in a transition from permeability reduction associated with faulting at shallow levels, to permeability enhancement at deeper levels (Scott and Nielson, 1991; Fisher et al., 2003, in press). The depth of the transition depends on burial history, geothermal gradient and sediment characteristics.

The observed porosity and pressure-dependence of deformation in porous rocks is similar to that of soils. Specifically, a porosity-dependent capped yield surface, coupled with a flow rule that predicts compaction and strain hardening in the ductile regime, and dilatant strain softening in the brittle regime, are key features of critical state soil mechanics (CSSM) (Roscoe and Burland, 1968; Schofield and Wroth, 1968; Atkinson and Bransby, 1978) that are broadly consistent with the behaviour of porous rocks. A number of authors have discussed the application of CSSM to porous rocks, using data from deformation experiments to illustrate the form of the yield surface and flow rule for specific rock types (e.g. Gerogiannopoulos and Brown, 1978; Graham et al., 1983; Elliott and Brown, 1985, 1986; Brown and Yu, 1988; Steiger and Leung, 1991; Wong et al., 1992; Bernabé et al., 1994; Wong et al., 1997; Ling et al., 2002; Cuss et al., 2003). This study takes a step further, by parameterising a critical state constitutive model for sandstone and implementing it in a numerical model, which is used to investigate the mechanical behaviour of sandstones in compressional and extensional tectonic settings. The numerical model permits quantitative investigation of the concepts discussed by Fisher et al. (2003, in press), including the feedback between mechanical deformation and fluid flow that arises from deformation-induced permeability variation.

The structure of this paper is as follows. We begin by outlining key features of CSSM to provide a framework for comparison with experimental data. The next section presents results of deformation experiments on sandstones, and shows how these may be used to parameterise a CSSM constitutive model. The numerical method is outlined, then the model is used to simulate deformation of sandstones in extensional and compressional regimes. We conclude with a discussion of the method and its limitations.

2. Cam Clay: a simple CSSM model

Our approach is based on the Modified Cam Clay constitutive model (Roscoe and Burland, 1968), which was derived from the original Cam Clay model of Schofield and Wroth (1968). The term ''Modified'' is dropped from now on. This constitutive model was chosen for its simplicity, particularly the smooth, continuous yield surface and associated flow rule, which are relatively easy to implement in a numerical code. Cam Clay does not capture every detail of porous rock behaviour, but it serves as a useful starting point for our numerical investigations.

The Cam Clay model is defined in terms of P (effective pressure), Q (second invariant of the effective deviatoric stress) and V (specific volume):

$$P = -\frac{1}{3}\sigma_{ii} \tag{1a}$$

$$Q = \sqrt{\frac{3}{2}s_{ij}s_{ij}} \tag{1b}$$

$$V = 1/(1-\phi) \tag{1c}$$

(see Table 1 for nomenclature; compressive stress is negative and Einstein summation applies). Note that specific volume (V) is an increasing function of porosity (ϕ). Q is equal to the differential stress in a standard ''triaxial'' test, where $\sigma_1 > \sigma_2 = \sigma_3$. The yield surface (also known as the Roscoe surface) is defined by:

$$Q^2 + M^2 P(P - P^*) = 0 \tag{2}$$

where P^* is the pressure corresponding to the onset of irreversible porosity reduction during hydrostatic (isotropic) loading, which is related to V according to Eq. (3):

$$V = V_\lambda - \lambda \ln P^* \tag{3}$$

Eq. (2) defines a semi-ellipse in the P, Q plane for a given value of P^* (Fig. 1a). The peak of the ellipse occurs at $(P,Q) = (P^*/2, MP^*/2)$, where M is a material property. The ellipse is closed on the P-axis at $P = 0$ and $P = P^*$; there is no cohesion or tensile strength. The yield surface forms an

Table 1
Nomenclature

Symbol	Definition (units)
A	Slope of ϕ versus $\log k$ curve for elastic loading/ductile yield (m^2)
CSL	Critical state line
d	Grain diameter (m)
f	Multiplier in porosity–permeability relationship
k	Permeability (m^2)
M	Value of Q/P at peak of Cam Clay yield envelope
m, n	Exponents in porosity–permeability relationship
NCL	Normal consolidation line
P	Effective pressure (Pa)
P^*	Onset of irreversible porosity reduction during hydrostatic loading (Pa)
P_{cr}	Effective pressure at peak of Cam Clay yield envelope; the brittle–ductile transition (Pa)
Q	Second invariant of effective deviatoric stress (Pa)
r	Grain radius (μm)
T	Temperature (°C)
t	Time (s)
V	Specific volume
V_λ	Specific volume at 1 Pa on the NCL
V_κ	Specific volume at 1 Pa on an elastic loading path
α	P_{cr}/P^*
ϕ	Porosity
ϕ_0	Porosity of undeformed rock
ϕ_t	Transition from permeability enhancement to permeability reduction during brittle yield
λ	Slope of NCL in V, $\ln P$ space (Pa^{-1})
κ	Slope of elastic loading/unloading paths in V, $\ln P$ space (Pa^{-1})
σ_{ij}	Effective stress tensor (Pa)
s_{ij}	Effective deviatoric stress tensor (Pa)

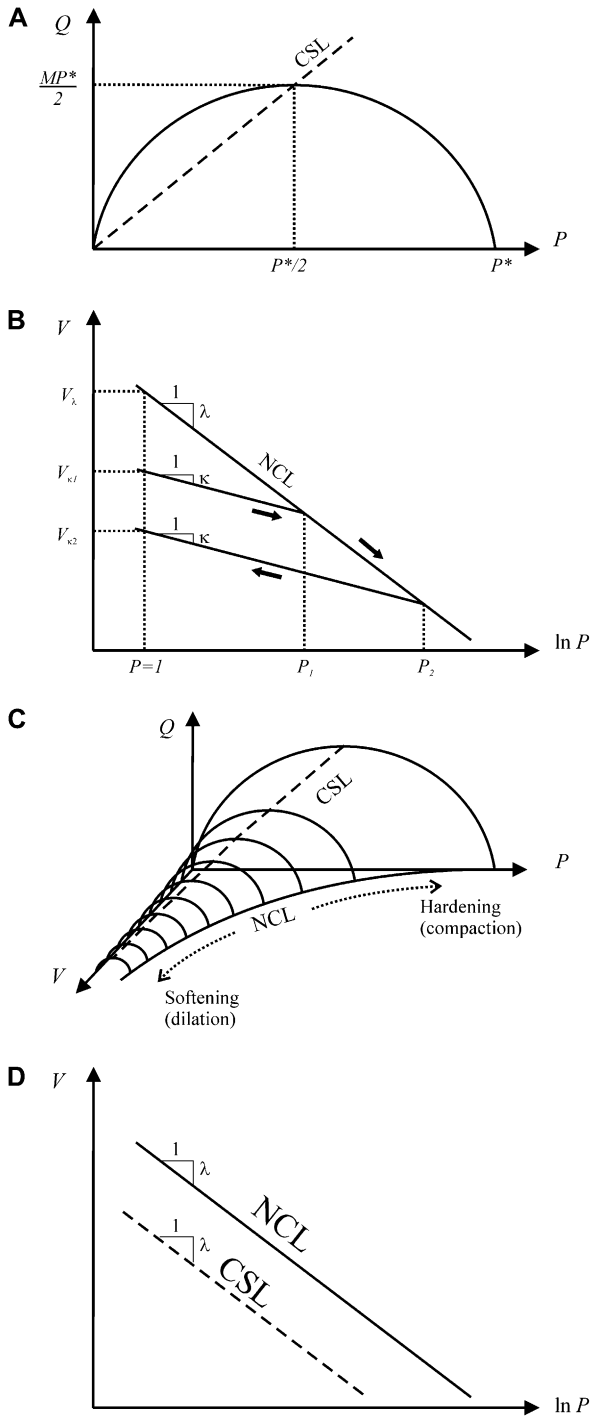

Fig. 1. Aspects of the Cam Clay yield surface. (A) Yield envelope and projection of the critical state line in P, Q space. (B) Elastic loading/unloading paths and normal consolidation line in V, ln P space. Arrows indicate path followed by a sample undergoing hydrostatic compression. The sample undergoes elastic compaction to $P = P_1$, then undergoes irreversible porosity reduction along the NCL to P_2, at which point it is unloaded and follows an elastic swelling line parallel to the initial elastic loading path. The position and slope of the NCL are defined by V_λ and λ, and that of the elastic loading/unloading lines by V_κ and κ. (C) Cam Clay yield surface in P, Q, V space. (D) NCL and CSL in V, ln P space.

ellipsoid in principal stress space, with the long axis along the line $\sigma_1 = \sigma_2 = \sigma_3$ and with one end at the origin. Eq. (3) defines the Normal Consolidation Line (NCL), where $-\lambda$ is the slope of the NCL in V versus ln P space, and V_λ is the specific volume on the NCL at unit pressure. Hydrostatic (isotropic) loading paths follow straight lines in V versus ln P space (Fig. 1b). A sample undergoing progressive hydrostatic loading follows an elastic loading path of slope κ until it reaches the NCL. The intersection of the elastic loading path with the NCL at $P = P^*$ defines the onset of irreversible porosity reduction for that loading path. The sample proceeds along the NCL, undergoing irreversible porosity reduction until it is unloaded, from which point it follows an elastic swelling line of slope κ. The equation of the elastic loading/swelling lines is:

$$V = V_\kappa - \kappa \ln P \tag{4}$$

where V_κ is the specific volume on the elastic loading line at unit pressure. There is an infinite number of elastic loading lines, with V_κ being determined by the current value of P^* (see Fig. 1b).

Fig. 1c shows the three-dimensional yield surface in Q, P, V space. The NCL bounds the yield surface on the plane $Q = 0$. The line that runs along the crest of the surface in Q, P, V space is known as the Critical State Line (CSL; dashed line in Fig. 1c). The projection of the CSL onto the Q, P plane is a straight line of gradient M, passing through the origin (Fig. 1a). The same line projected into V, ln P space forms a straight line parallel to the NCL (Fig. 1d).

The Cam Clay model uses an associated flow rule, with the plastic potential function being the same as the yield function; hence, strain increment vectors are normal to the yield surface (Drucker, 1951; Hobbs et al., 1990). Yielding on the left-hand side of the envelope ($P < P^*/2$) results in dilation and strain softening (P^* decreases), whereas yielding on the right-hand side ($P > P^*/2$) results in shear-enhanced compaction and strain hardening (P^* increases). There is a smooth gradation between these two behaviours, with the volumetric strain increment vanishing at the peak of the envelope. The yield envelope in the Q, P plane shrinks during strain softening, and expands during strain hardening, hence the stress state always migrates towards the CSL (i.e. the peak of the yield envelope) during progressive loading. A sample that reaches the CSL is said to be at critical state, from which point it can develop unlimited shear strain at constant Q, P, and V.

We use the terms brittle and ductile to describe the macroscopic behaviour of samples that undergo dilatant shear failure on the left-hand side of the yield envelope, and shear-enhanced compaction on the right-hand side of the yield envelope, respectively. This terminology is not intended to imply anything about the underlying deformation mechanism; macroscopically ductile behaviour may involve cataclasis and/or true crystal plasticity, depending on temperature, mineralogy and water content (Paterson and Wong, 2005). The term ‘‘transitional regime’’ will be used to refer to yield that occurs at or close to the peak of the yield envelope.

3. Experimental data

In this section we compare data from hydrostatic and triaxial tests on porous sandstones with the Cam Clay constitutive model. In particular we evaluate non-linear elasticity, the shape of the yield envelope, hardening/softening associated with volumetric strain, and attainment of critical state at high strain. Other authors have explored the porosity-dependent yield behaviour of limestone (e.g. Celle and Cheatham, 1981; Elliott and Brown, 1985; Baud et al., 2000; Vajdova et al., 2004), chalk (e.g. Brown and Yu, 1988; Homand and Shao, 2000; Collin et al., 2002) and shale (e.g. Graham et al., 1983; Steiger and Leung, 1991). This study focuses on the behaviour of sandstones.

We have deliberately chosen a simple constitutive model for this investigation, although a number of more sophisticated models have been described in the literature. For example, Collins and Hilder (2002) and Bigoni and Piccolroaz (2004) derived generalised yield functions from which classical constitutive models, such as Cam Clay, can be recovered by appropriate choice of parameter values. Ling et al. (2002) developed an anisotropic critical state model which includes rotational and distortional hardening rules, in addition to the volumetric (isotropic) hardening rule of Cam Clay. Other authors have discussed the role of the third stress invariant, which is not considered in the Cam Clay model, and the need for a non-associated flow rule to describe certain aspects of porous rock behaviour (e.g. Roscoe and Burland, 1968; Lubarda et al., 1996; Collin et al., 2002; Collins, 2003; Borja and Aydin, 2004). A simple constitutive model is preferred here, not only for ease of numerical implementation, but also to minimise the number of parameter values that must be determined in order to apply the model.

3.1. Sandstones: mechanical behaviour

Zhang et al. (1990) performed hydrostatic compression tests on a suite of sandstones with porosities ranging from 5 to 35%, each of which showed an inflection point in the loading curve corresponding to the onset of cataclasis. Loading beyond this critical effective pressure (P^*) resulted in accelerated, irreversible porosity reduction, with subsequent unloading following a path broadly parallel to the initial elastic loading curve. P^* was shown to decrease systematically with increasing porosity (ϕ) and grain radius (r), conforming to a linear relationship in $\log(\phi r)$ versus $\log P^*$ space (Zhang et al., 1990). This relationship has subsequently been confirmed for several additional sandstones (e.g. Zhu and Wong, 1997; Cuss et al., 2003). On the basis of these results, Fisher et al. (2003, in press) suggested the following equation to derive values of P^* for sandstones of varying porosity and grain size:

$$\log P^* = -1.1 \log(\phi r) + 3.5 \quad (5)$$

where P^* is in MPa and r is the grain radius in μm. The line given by Eq. (5) forms a lower bound to the experimental data (Fig. 2a). Using this lower bound in our model compensates for the fact that P^* has been plotted against the *initial* porosity of the rock, rather than the porosity at $P = P^*$, which is slightly less than the original porosity due to elastic compaction.

The normal consolidation line of the Cam Clay model is defined by a linear relationship between V and $\ln P^*$ (Fig. 1b, Eq. (3)). Eqs. (3) and (5) both predict a decrease in P^* with increasing porosity, but grain size does not appear in Eq. (3). Eq. (5) does not correspond to a set of straight lines in V, $\ln P$ space (see Fig. 2b), so is not equivalent to the NCL of the Cam Clay model. However, the data points shown in Fig. 2a define a broadly linear trend in V, $\ln P$ space (Fig. 2b), consistent with the NCL (Eq. (3)). The slope of a linear best-fit line through these data is −0.15; this is taken to correspond to $-\lambda$ in the Cam Clay model.

Loading paths from individual compression tests can be used to derive values of λ and κ for specific samples. This approach is illustrated in Fig. 3, which shows linear loading paths superimposed on hydrostatic test data for eight sandstones. Corresponding values of λ and κ are listed in Table 2. Loading and unloading paths defined by these data can be approximated by straight lines in V, $\ln P$ space, although the elastic loading paths tend to curve downwards before joining the normal consolidation line. λ cannot be defined for

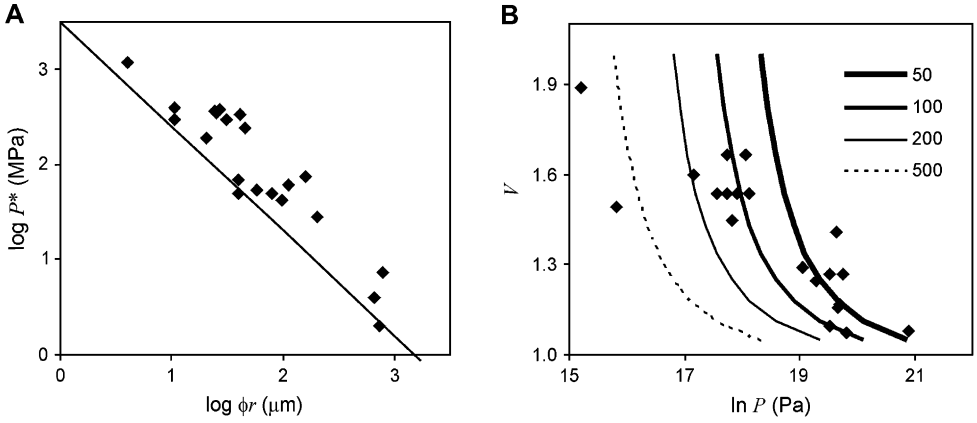

Fig. 2. Values of P^* from hydrostatic compression tests on porous rocks. Data from Wong et al. (1997). (A) Data in $\log P^*$ versus $\log \phi r$ space. Straight line corresponds to Eq. (5). (B) Data in V versus $\ln P^*$ space. Curves correspond to Eq. (5) (grain radii indicated in μm).

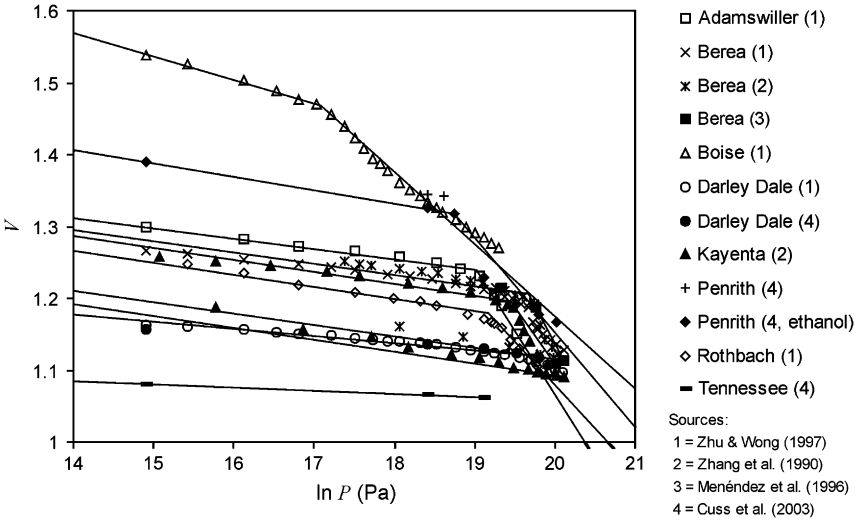

Fig. 3. Hydrostatic test data and inferred linear loading paths for eight sandstones. Corresponding parameter values listed in Table 2.

Tennessee sandstone because the test did not reach P^* (Cuss et al., 2003). Data for Darley Dale sandstone are ambiguous; Cuss et al. (2003) considered that their tests on this sandstone did not reach P^*, whereas Wong et al. (1997) interpreted a value of $P^* = 360$ MPa from the data of Zhu and Wong (1997).

The value of λ determined from the linear best-fit line to data in Fig. 2b has been included in Table 2 for comparison. This value is the same as the average of the independently-determined values of λ for individual sandstones. The coincidence of these values suggests that compiling data from sandstones with different porosities and grain size is a valid approach to parameterise the hydrostatic deformation of sandstones in general.

Complete specification of the NCL requires a known point on the line in addition to its slope. An obvious approach is to use the intersection of the initial elastic loading path with the NCL, which is the initial value of P^*. We have chosen instead to use Eq. (5) to locate the NCL in V, ln P space, taking values of λ and κ from the loading paths of hydrostatic tests (Table 2). This approach incorporates grain size dependence into the constitutive model (although grain size is assumed to remain constant during deformation), and allows for the tendency of rocks to be weaker in nature than in experiments.

Table 2
Cam Clay parameters for 8 sandstones

Name	Porosity (%)	Grain radius (mm)	κ	λ	M	α
Adamswiller	22.6	0.09	0.014	0.18	1.3	0.5
Berea	21	0.13	0.016	0.21	1.15	0.45
Boise	35	0.28	0.033	0.10	1.5	0.55
Darley Dale	14.5	0.17	0.010	–	1.15	0.45
Kayenta	21	0.15	0.017	0.16	1.3	0.5
Penrith	28	0.06	0.019	0.13	1.2	0.5
Rothbach	19.9	0.23	0.017	0.12	1.2	0.5
Tennessee	7.5	0.04	0.005	–	1.1	0.45
Average			0.016	0.15	1.2	0.5
Best-fit Fig. 2b				0.15		

The next step in our analysis is to compare the shape of the yield envelope for sandstones with that of the Cam Clay model. Fig. 4 shows yield data in Q, P space from triaxial (Khan et al., 1991; Wong et al., 1997) and hydrostatic (Zhang et al., 1990; Zhu and Wong, 1997) compression tests on Berea sandstone. Also shown are the Roscoe envelope (dashed line) and an alternative yield envelope (solid line). Data for ductile yield are rather scattered, and both envelopes provide a reasonable fit to the data. However, the Roscoe envelope consistently overestimates the yield stress in the brittle regime, and the alternative yield envelope provides a better fit. The alternative yield envelope is defined by two equations:

$$Q^2 - \frac{QP^*M}{2}\left[1 - \left(\frac{P}{P_{cr}} - 1\right)^2\right] = 0 \text{ for } P \le P_{cr} \tag{6a}$$

$$Q^2 - \left(\frac{MP^*}{2}\right)^2\left(1 - \left(\frac{P - P_{cr}}{P^* - P_{cr}}\right)^2\right) = 0 \text{ for } P \ge P_{cr} \tag{6b}$$

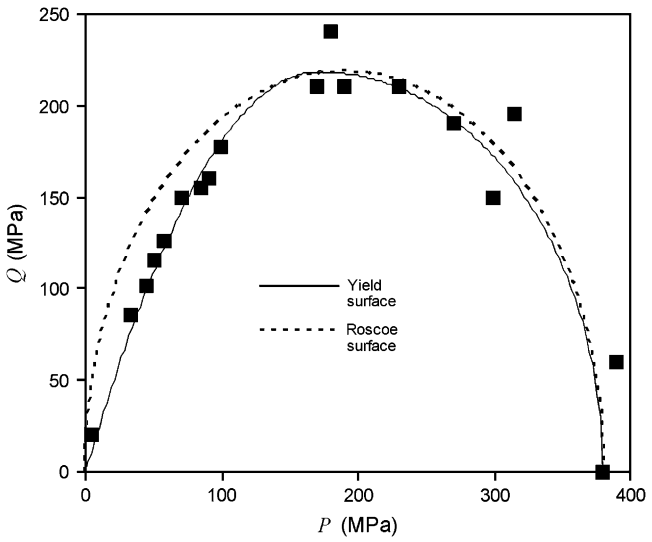

Fig. 4. Yield envelope for Berea sandstone.

where P_{cr} is the effective pressure at the peak of the envelope. Eqs. (6a) and (6b) are modified versions of the equations suggested by Wong et al. (1997) and discussed further by Cuss et al. (2003) to fit yield data from a number of sandstones. Our modifications force the envelope to pass through $(P,Q) = (0,0)$, and ensure that the equations have the same value and a slope of zero in P, Q space when $P = P_{cr}$, resulting in a smooth, continuous yield envelope with continuously varying gradient in P, Q space. The Cam Clay model uses an associated flow rule, which requires strain increment vectors to be normal to the yield envelope (the normality condition; Drucker, 1951). This implies that the volumetric strain increment vanishes at the peak of the yield envelope (where its slope is zero), hence $P = P_{cr}$ represents the transition from dilation to compaction. The validity of the associated flow rule for sandstones is discussed further below. Defining $\alpha = P_{cr}/P^*$, we note that Eq. (6b) is identical to the Roscoe surface (Eq. (2)) when $\alpha = 0.5$. The yield surface shown in Fig. 4 was obtained with $M = 1.15$ and $\alpha = 0.45$.

Fig. 5 shows yield envelopes defined by Eqs. (6a) and (6b) fitted to yield data from eight sandstones (Khan et al., 1991; Zhu and Wong, 1997; Wong et al., 1997; Cuss et al., 2003). Corresponding values of M and α are listed in Table 2. Some of the yield envelopes are rather poorly constrained, especially that of Tennessee sandstone for which no data were obtained in the ductile regime. Penrith sandstone displays anomalous behaviour and the yield envelope is not clearly defined.

The preceding analysis is based on results of compression tests, where P increases during the course of the test. Zhu et al. (1997) obtained similar results from experiments following a different loading path, in which the axial load was maintained while the radial load was increased. Most sedimentary basins form in extensional tectonic settings, where P may decrease during the course of deformation. In the absence of deformation tests following such a loading path, some insight into likely behaviour of sandstones in extensional regimes can be gained by considering the relationship between the Cam Clay yield surface and the Mohr Coulomb failure criterion. Wood (1990) showed that the Mohr Coulomb failure envelope corresponds to the critical state line of the Cam Clay model, for the case of a material with zero cohesion and zero tensile strength. Following this argument, it is possible to derive expressions for M as a function of the friction angle, and it can be shown that these expressions are different for triaxial compression ($\sigma_1 > \sigma_2 = \sigma_3$) and triaxial extension ($\sigma_1 < \sigma_2 = \sigma_3$). Wood (1990) goes on to argue that, as the friction angle is usually the same in extension and compression, M is expected to be different for the two loading paths (it is smaller in extension than in compression). For example, a friction angle of 30° gives $M = 1.2$ in compression and $M \sim 0.857$ in extension.

We now consider the post-yield behaviour of sandstones under anisotropic (non-hydrostatic) loading conditions. In particular, we aim to determine whether the associated flow rule is applicable to sandstones, and whether sandstones display critical state behaviour. Attainment of critical state is indicated when there is no further change in ϕ, P and Q with continuing deformation. Laboratory experiments rarely go to sufficiently high strain to attain critical state, especially in the brittle regime where macroscopic failure is likely to occur before this point can be reached. Nonetheless, some experimental results appear to be consistent with the critical state concept. For example, stresses recorded at high strain in experiments on Penrith, Darley Dale and Tennessee sandstones plot on or close to the projection of the inferred CSL in P, Q space (Cuss et al., 2003). This observation does not constitute proof of critical state behaviour, but it confirms that the stress state evolves towards the CSL during progressive deformation.

Wong et al. (1992) tracked the post-yield evolution of P, Q and ϕ in Berea sandstone in the ductile regime. Fig. 6 shows the stress state at porosities of 16, 13, 10.5 and 8% during six triaxial tests starting at confining pressures ranging from 100 to 450 MPa (Wong et al., 1992). Crosses indicate the peak stress attained by preloaded samples that failed in the brittle regime; these samples underwent isotropic loading to $P > P^*$, and were then partially unloaded before commencing

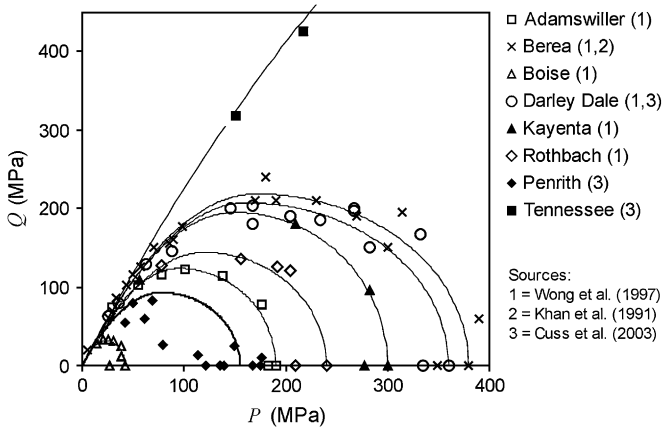

Fig. 5. Triaxial and hydrostatic test data and inferred yield surfaces for eight sandstones.

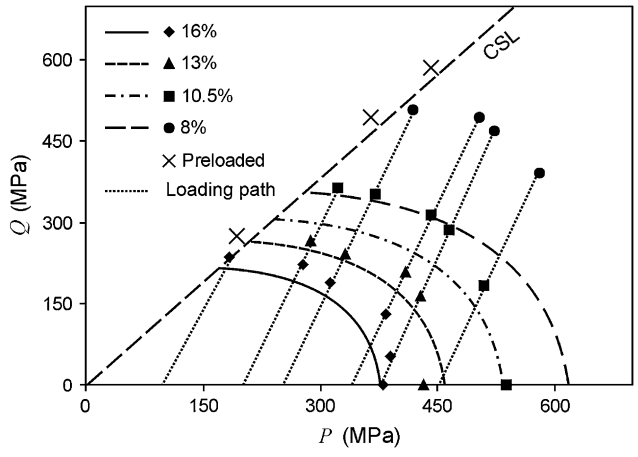

Fig. 6. Progressive loading of Berea sandstone beyond initial yield (data from Wong et al., 1992). Solid symbols indicate stress state at porosities of 16, 13, 10.5 and 8% along six triaxial loading paths in the ductile regime. Crosses indicate peak stress attained by samples loaded hydrostatically to 540 MPa, then partially unloaded to 100, 200 and 250 MPa before commencing triaxial compression. Curves = yield envelopes derived from Eq. (6b) using parameter values in Table 2.

triaxial compression. The curved lines indicate ductile yield envelopes corresponding to each porosity value, calculated from Eq. (6b) using parameter values from Table 2. The CSL is shown as a long-dashed line. Agreement between the predicted yield envelopes and data points is poor, although the position and slope of the CSL is reasonable, as it separates data from samples that underwent ductile yield from those that underwent brittle failure. An improved fit could be obtained by adjusting the values of M, λ, and α, but it is difficult to find parameter values that agree with all data points.

Our difficulty in fitting yield envelopes to post-yield data suggests that associated plasticity and the simple volumetric strain hardening rule of our Cam Clay model may be an oversimplification for porous sandstones. Indeed, this is consistent with several other studies that have questioned the validity of the associated flow rule, especially for yield in the brittle and transitional regimes (Celle and Cheatham, 1981; Graham et al., 1983; Elliott and Brown, 1985; Wong et al., 1997). This point is considered further in the discussion section.

3.2. Sandstones: permeability

A modified form of the Kozeny–Carman equation (Eq. (7); see Table 1 for nomenclature) provides a good approximation to the porosity–permeability relationship in undeformed sandstones and other sedimentary rocks (Oelkers, 1996).

$$k = \frac{fd^2\phi^n}{(1-\phi)^m} \tag{7}$$

Eq. (7) gives a good fit to porosity–permeability data from various sandstones (Ehrenburg, 1990; Harrison and Summa, 1991; Oelkers, 1996; Kieffer et al., 1999) with values of n ranging from 3 to 7, f ranging from $\sim 10^{-2}$ to $\sim 10^{-4}$, and $m = 2$.

The relationship between porosity and permeability deviates markedly from Eq. (7) during deformation, as illustrated in Fig. 7A, which shows porosity–permeability evolution during isotropic and triaxial loading of Rothbach sandstone (Zhu and Wong, 1997), along with a curve corresponding to Eq. (7). The observed reduction in permeability during ductile yield is consistent with measured permeability contrasts between natural cataclastic faults and their host rocks (e.g. Antonellini and Aydin, 1994; Fisher and Knipe, 2001), although natural fault rocks can display more extreme permeability reduction due to post-failure cementation. Permeability evolution during elastic loading and ductile yield can be approximated by a linear relationship between porosity and log permeability (c.f. Morris et al., 2003), as illustrated in Fig. 7B. Some experimental results show an increase in the rate of permeability reduction at the onset of ductile yield (Zhu and Wong, 1997); we have not attempted to represent this behaviour in our model.

Permeability evolution in the brittle regime depends on the initial porosity of the host rock. Experimental results indicate that permeability *decreases* with increasing porosity during brittle failure of high porosity sandstone (triangles in Fig. 7A), reflecting an increase in tortuosity and/or decreased connectivity of the pore network (Zhu and Wong, 1997; David et al., 2001). This contrasts with the behaviour of low porosity rocks, which display a marked *increase* in permeability during failure in the brittle regime (e.g. Zhu and Wong, 1999). To quantify the evolution of permeability in the brittle regime we assume a linear relationship between porosity and log permeability, with the slope of the line being a linear function of initial porosity (ϕ_0) such that permeability increases with dilation in low porosity rocks, and decreases with dilation in high porosity rocks (Fig. 7B). The transition from permeability increase to permeability decrease occurs at $\phi_0 = \phi_t$. Experimental results for a range of sandstones suggest that ϕ_t should be <0.15, but this is not well constrained.

Our method for calculating permeability can be summarised as follows. The initial permeability k_0 is obtained from

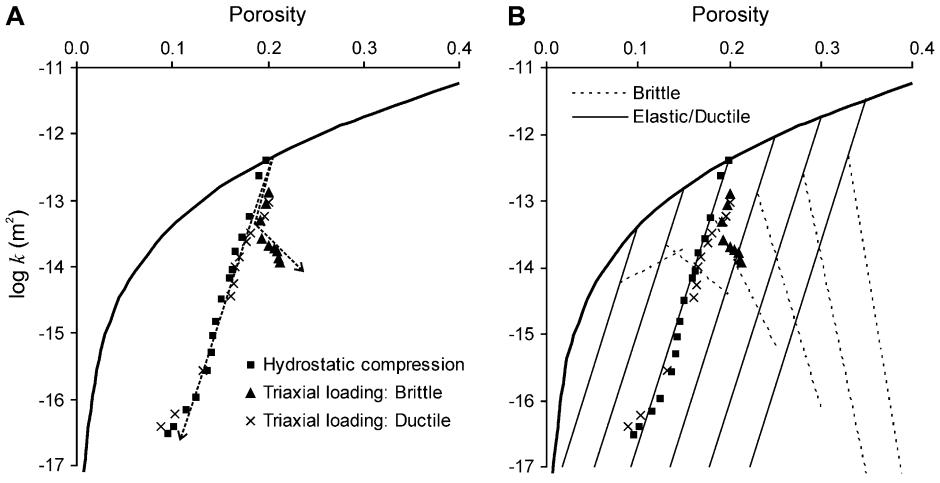

Fig. 7. Porosity–permeability evolution during deformation. (A) Rothbach sandstone; data from Zhu and Wong (1997). Solid curve represents Eq. (7) with $n = 3$, $m = 2$, $f = 1.58 \times 10^{-4}$ and $d = 4.6 \times 10^{-4}$ m. Arrows indicate direction of loading path. (B) Parameterisation of porosity–permeability evolution during deformation. Data from Fig. 7A shown for comparison. Solid lines correspond to Eq. (8a), dashed lines correspond to Eq. (8b). Initial permeability given by Eq. (7), heavy solid line. Transition from permeability increase to permeability decrease with dilation occurs at $\phi_t = 12\%$, indicated by change from positive to negative slope of brittle failure curves (dashed lines) between $\phi_0 = 10\%$ and $\phi_0 = 15\%$.

Eq. (7), using known values of porosity, permeability and grain size from an undeformed specimen to determine the value of f. During elastic loading/unloading and ductile yield, permeability is given by:

$$\log k = A(\phi - \phi_0) + \log k_0 \tag{8a}$$

where A is the slope of a linear best-fit line through ϕ versus $\log k$ data (e.g. Fig. 7B), and ϕ_0 is the porosity at the onset of deformation. During brittle failure, Eq. (8a) is replaced by:

$$\log k = A\left(1 - \frac{\phi_0}{\phi_t}\right)(\phi - \phi_1) + \log k_1 \tag{8b}$$

where k_1 and ϕ_1 are the permeability and porosity at the onset of brittle failure. These relationships are illustrated in Fig. 7B. Note that we ignore the effects of cementation, clay smears, and fault gouge (grain size reduction), which are known to have a significant impact on fault permeability (e.g. Fisher and Knipe, 1998).

4. Numerical model

Cam Clay is one of several constitutive models available in FLAC3D, a commercial finite difference code for solving coupled deformation and fluid flow problems in engineering and rock mechanics (Cundall and Board, 1988; Itasca Consulting Group, 2002). The existing code was modified to incorporate the sandstone yield function (Eqs. (6a) and (6b)) and corresponding potential function, assuming an associated flow rule. This was achieved through the "user-defined constitutive model" functionality in FLAC3D, which enables the user to define a new constitutive model in C++. Fluid flow is described by Darcy's law, which is solved in conjunction with a continuity equation for the fluid. Initial permeability is calculated from Eq. (7), and evolves as a function of porosity during deformation according to Eqs. ((8a) and (8b)). Mechanical and fluid flow calculations are coupled in the sense that deformation induces changes in fluid pressure and permeability due to changes in porosity, and fluid pressure influences deformation through its impact on effective stress. The model does not allow negative effective pressure, and the material has no cohesion or tensile strength.

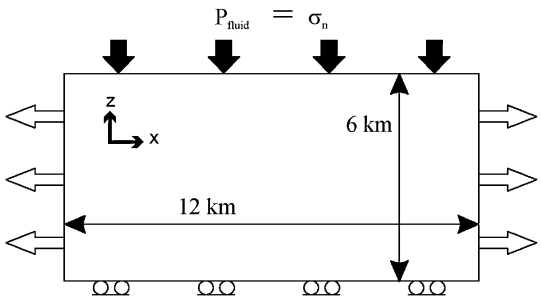

Fig. 8. Initial and boundary conditions for the numerical model.

5. Initial and boundary conditions

Results presented in this paper represent deformation of part of a sedimentary basin that is initially 12 km wide by 6 km deep (Fig. 8). The model is discretized onto a mesh comprising 120 hexahedral zones in the x-direction, 60 zones in the z-direction, and one zone in the y-direction. The stress–strain response is calculated in three dimensions, but the present investigation focuses on 2D plane strain scenarios with no movement in the y (out-of-plane) direction. The base of the model is free to move in the x-direction and fixed in the z-direction, and the sides are moved inwards (compression) or outwards (extension) at a constant velocity in the x-direction. The top boundary is treated as if the model was overlain by a body of water, with the water surface (i.e. sea level) remaining fixed in space, while the model boundary is free to move up or down and develop topography. The effect of overlying water is represented by applying a pressure on the top boundary to represent the weight of overlying water, which varies over time as the top of the model moves relative to sea level. Effects of erosion and deposition during deformation are not represented in this model. Fluid is free to move across the top and base of the model, and the sides are impermeable.

Note that the constitutive model has been parameterised using results of "triaxial" (axisymmetric) compression tests in which the third stress invariant reduces to zero. We assume that the predictions of this model are valid in non-axisymmetric scenarios (specifically plane strain), but this has not been verified.

The initial porosity–depth distribution is determined by an algorithm representing deposition and progressive porosity reduction due to gravitational compaction and quartz cementation. Following the approach of Fisher et al. (2003, in press), we use the method of Walderhaug (1996) to calculate the volume fraction of quartz cement as a function of burial rate, geothermal gradient and grain size. Progressive deposition and burial are simulated using a one-dimensional column that is one zone wide in the x and y-directions, with additional zones added one at a time to the top of the model, representing newly deposited sediment. The column undergoes uniaxial strain; there is no displacement in the x or y directions during deposition. The algorithm for deposition, cementation and compaction is as follows: (1) add one new zone to top of model and assign Cam Clay properties; (2) update temperature for each zone, based on new depth and specified geothermal gradient; (3) add quartz cement to each zone in accordance with the burial rate; (4) allow the model to equilibrate under gravity (compaction and fluid flow); (5) repeat steps 1–4 until desired model height is reached; (6) Copy properties of the 1D column (porosity, density, fluid pressure, etc.) onto the 2D mesh. Gravitational compaction occurs during step 4; the top of the model sinks downwards as compaction takes place, until a new equilibrium stress state is attained. It is important to note that the column behaves as a Cam Clay material during compaction, and does not necessarily remain in an elastic state. This is where our approach differs from that of Fisher et al. (2003, in press), who used the same cementation model

to calculate porosity–depth curves without considering the effects of gravitational compaction. Based on these porosity–depth curves, they used Eq. (5) to calculate P^* as a function of porosity and grain size, and estimated the value of P/P^* at yield in an extensional regime, assuming lithostatic loading and hydrostatic fluid pressure. The limitation of their approach is that it is somewhat decoupled from the constitutive behaviour of the rock, and hence allows development of stress states that lie outside the yield surface (e.g. $P/P^* > 1$). Step 4 in our deposition algorithm prevents the development of such impossible stress states, with ductile yield occurring when the stress state reaches the yield envelope.

Compaction and permeability reduction during burial result in the pore fluid being slightly overpressured towards the base of the model. This results in slow upward flow, which in reality may be enhanced by several processes that are not represented in the model, such as dehydration reactions and thermal effects (e.g. Bethke, 1985; Harrison and Summa, 1991). We account for these additional processes by adjusting the fluid pressure gradient after initialisation to give a uniform upward fluid flux throughout the model, then fixing the fluid pressure at the base of the model.

6. Results

The range of conditions encountered in sedimentary basins defines a large parameter space that could be investigated using our numerical model. Here we present a selection of results obtained from various combinations of two deposition rates (50 and 500 m/Ma), two geothermal gradients (20 and 30 °C/km), and two grain radii (100 and 200 μm). The ends of the model were moved at a constant velocity of 6×10^{-10} m/s, representing an initial longitudinal strain rate of 10^{-13} s^{-1}. This relatively high strain rate is necessitated by the explicit formulation of FLAC3D, which makes it difficult to achieve sufficiently large strain to demonstrate the behaviour of interest within a reasonable computational timeframe at a lower strain rate. However, it should be emphasised that the mechanical formulation itself is not time-dependent; it is only the coupling with fluid flow that necessitates consideration of time.

The position of the normal consolidation line in V, ln P space was determined by using Eq. (5) to calculate P^* based on a depositional porosity of 30%, with V_λ derived from Eq. (1c). The porosity–permeability relationship was parameterised using data from Zhu and Wong (1997) for Rothbach sandstone (f calculated by substituting $\phi = 0.20$ and $k = 4.079 \times 10^{-13}$ m^2 into Eq. (7) with $n = 3$, $m = 2$; $A = 43$ determined from best-fit line through porosity–permeability data during hydrostatic compression; ϕ_t estimated at 0.12). Cam Clay parameters were set to $M = 0.7$ (extension), $\alpha = 0.45$, $\lambda = 0.15$ and $\kappa = 0.016$. Fluid pressure was adjusted following initialisation to give a uniform upward flux of 10^{-10} m^3/m^2/s, consistent with estimates of the regional fluid flux due to metamorphic devolatilisation (Thompson, 1997).

Fig. 9 shows porosity–depth curves and the distribution of P/P^* with depth following initialisation. The rate of porosity reduction with depth depends on grain size, deposition rate, and geothermal gradient, because these factors control the cementation rate, but there is very little difference between models in the first 2 km of burial as the temperature is too low for significant cementation to take place. Both P and P^* increase with depth (P^* increases with decreasing porosity; P depends on the overburden), but they change at different rates, hence the ratio P/P^* varies with depth (Fig. 9B, D; Fisher et al., 2003, in press). Decreasing grain size reduces the value of P/P^* over the entire depth range of the model, because P^* is negatively correlated with grain size (Eq. (5)). Geothermal gradient and deposition rate influence P/P^* at depths greater than ~2 km, where their impact on cementation becomes important. Vertical dashed lines in Fig. 9B and D indicate the transition from brittle to ductile behaviour ($P/P^* = \alpha = 0.45$). Note that the curves in Fig. 9 represent the *initial* distribution of P/P^*; the value of P/P^* *at yield* depends on the loading path (extension or compression; see Fig. 10). A rock that starts with $P/P^* > \alpha$ may reach the yield envelope in the brittle regime during extension, because the loading path has negative slope in Q versus P space. Conversely,

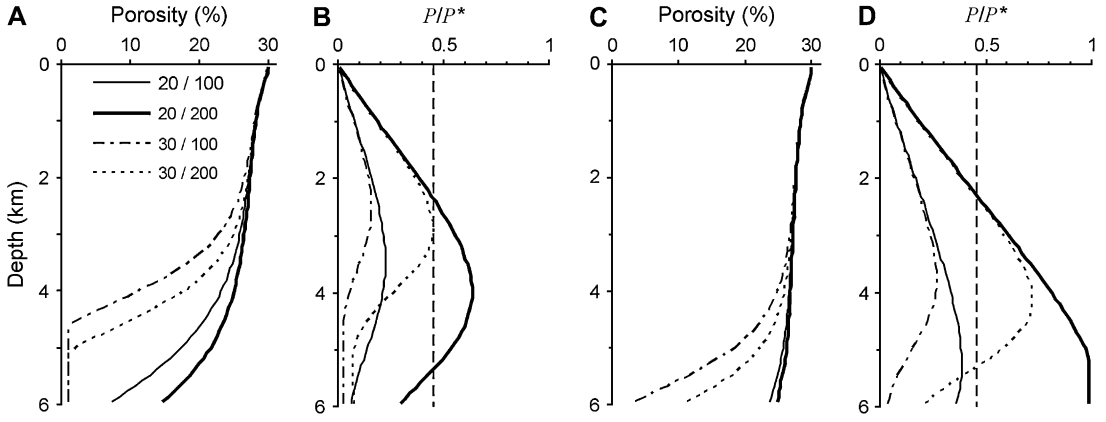

Fig. 9. Porosity and P/P^* versus depth following initialisation. Deposition rate = 50 m/Ma (A and B), 500 m/Ma (C and D). Legend refers to geothermal gradient (°/km) and grain radius (μm). Vertical dashed lines in B and D indicate the brittle–ductile transition ($\alpha = 0.45$).

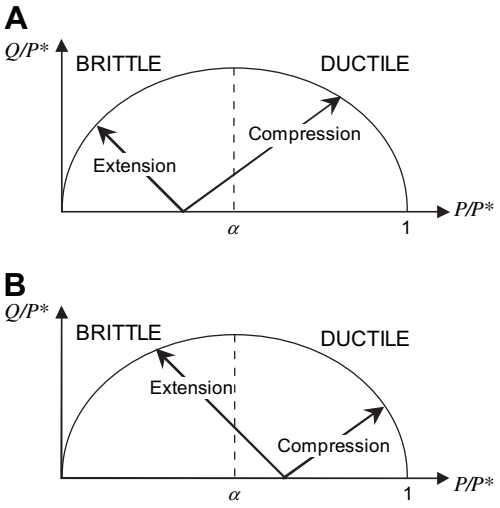

Fig. 10. Effect of loading path and initial P/P^* ratio on failure mode. (A) P/P^* initially less than α. (B) P/P^* initially greater than α.

a rock that starts in the brittle field may reach the ductile part of the yield envelope during compression (loading path has positive slope in Q versus P space). For a given porosity–depth distribution, this means that ductile behaviour occurs over a greater depth range in compressional regimes than in extensional regimes.

Fig. 11 shows the spatial distribution of shear and volumetric strain, permeability (m^2), and the ratio of permeability to its initial value after 1.5% extension for five different combinations of deposition rate, geothermal gradient and grain size. Models will be referred to by the letters used in Fig. 11 (A–E). Models A and E remain entirely within the brittle regime. Strain softening associated with dilatant shear failure results in spontaneous localisation, creating conjugate shear zones of finite width (Fig. 11A, E). The absolute width of these shear zones is not meaningful because there is no lengthscale in the mechanical formulation; a coarser mesh produces wider shear zones, but the qualitative behaviour is unchanged. The initial distribution of porosity and P/P^* is quite different in Models A and E (Fig. 9A, B); P/P^* is higher in Model A from 0 to ~4.2 km depth, then the curves cross over such that P/P^* is lower in Model A than in Model E. The flow rule dictates that the volumetric strain increment vanishes at the peak of the yield envelope ($P/P^* = \alpha$), hence volumetric strain is smallest in the central part of Model A, where P/P^* is closest to α. Model E has less variation in P/P^* with depth, and hence shows little variation in volumetric strain with depth.

The shear zones in Models A and E are less permeable than their host rocks, except towards the base of the model where porosity is sufficiently low to allow permeability enhancement during brittle failure (Fig. 11A, E). The difference in permeability distributions between these models is due to the difference in their initial porosity–depth distributions (Fig. 9B). Model A satisfies the conditions for permeability enhancement over a greater depth range than does Model E. Permeability enhancement is most easily identified from a plot of permeability divided by its initial value at a given depth (right-hand column of Fig. 11). This plot shows that permeability has increased ~100 times in the lower parts of the shear zones in Model A, while it has decreased by a similar amount towards the top of the model. The *change* in permeability is more important than the absolute value of permeability; a fault cutting through low porosity sandstone at 5 km depth may be significantly more permeable than its host rocks, but still less permeable than unconsolidated sand at shallower depth. This is demonstrated in Fig. 12, which shows fluid flow vectors in Model A. Fluid is focused into and along the shear zones where they are more permeable than the surrounding rock, but it diverges out of the shear zones at the point where they become less permeable than the host rock.

Comparison of Models B and C with Model A (Fig. 11) illustrates the effect of decreasing the geothermal gradient and increasing the deposition rate, respectively. These models have higher initial porosity than Model A, corresponding to higher initial values of P/P^* (Fig. 9). The extensional loading path intersects the yield envelope close to its peak ($P/P^* \sim \alpha$) at intermediate depths (~2–4 km), resulting in volumetric strains close to zero in this region. Deformation is less strongly localised in this area than in the dilatant, brittle regions above and below. The shear zones in these models are less permeable than their host rocks at all depths, because the porosity is too high to allow permeability enhancement.

The effects of decreasing geothermal gradient and increasing deposition rate are combined in Model D, in which P/P^* is greater than α over more than half of the depth range (Fig. 9D). Spatial distributions of shear and volumetric strain (Fig. 11D) suggest that localisation has not occurred in this model, although the upper half meets the yield envelope in the dilatant, brittle regime. Plots of shear and volumetric strain *rate* (Fig. 13) show that localised, brittle failure does in fact occur in the upper part of this model, with distributed shear-enhanced compaction in the lower part. It appears that strain hardening in the lower half of this model inhibits stabilisation of dilatant shear zones in the upper part, such that no individual shear zone can develop sufficient shear or volumetric strain to be identifiable on a plot of total strain (Fig. 11D).

Previously it was noted that shear-enhanced compaction is more likely to occur in compression than in extension, for a given combination of parameter values. This is illustrated in Fig. 14, which shows the distribution of shear and volumetric strain after 5.5% *shortening* in a model with the same parameter values as Model A, with the exception of M which was increased to 1.1 in accordance with expected variation of this parameter between extensional and compressional regimes. The results are shown at a higher strain than those for Model A (cf. Fig. 11A, 1.5% extension), because the compressional loading path takes longer to reach the yield envelope (Fig. 10A). Model A displayed dilatant, brittle behaviour over the entire depth range of the model in extension, but compressional loading places the model in the ductile regime over part of its depth range.

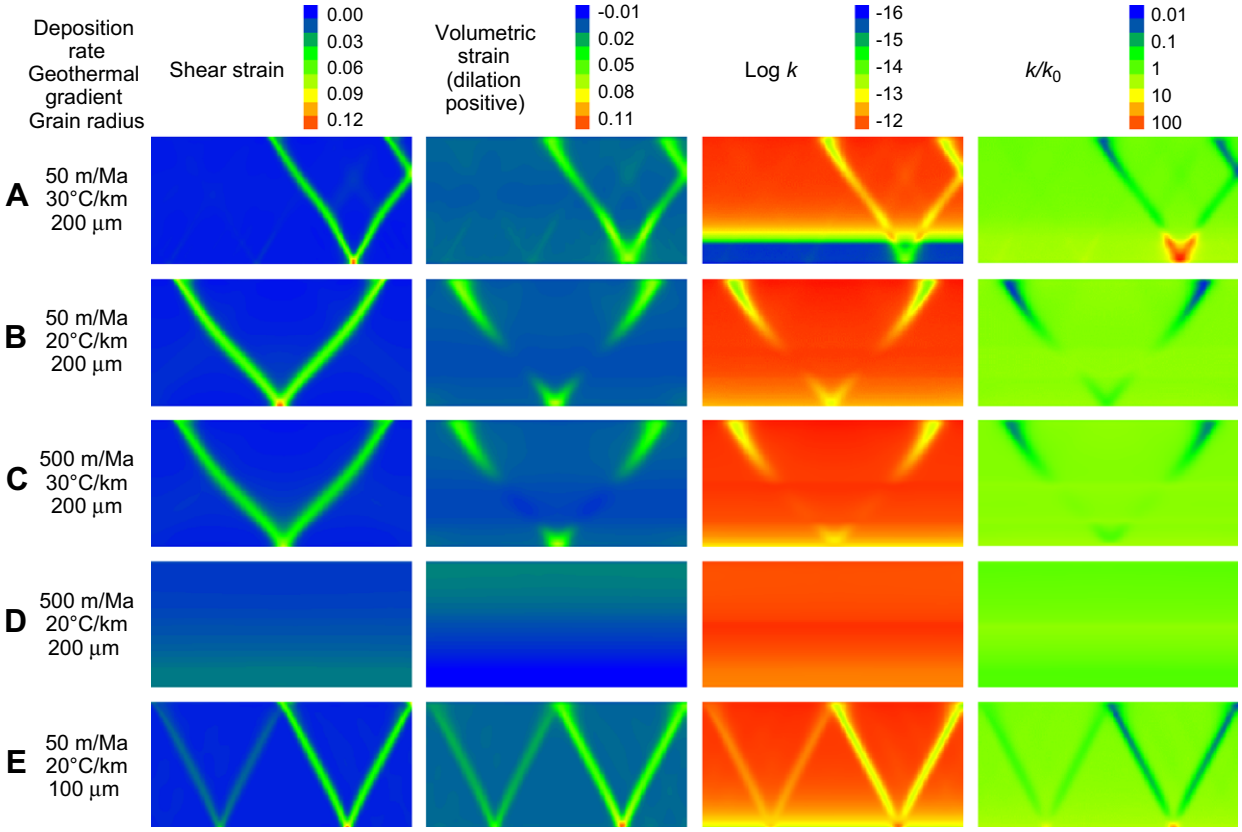

Fig. 11. Distribution of shear and volumetric strain, permeability, and permeability/initial permeability after 1.5% extension. Width of model = 12.18 km.

7. Discussion

Focused fluid flow requires localised deformation and increased permeability, which (in porous sandstones) is only possible in the brittle regime ($P/P^* < \alpha$), and then only if the initial porosity is less than ~15%. Table 3 lists the depth at which these conditions are first met for the scenarios shown in Fig. 9, based on the distribution of porosity and P/P^* following initialisation. For the range of parameter values investigated here, the shallowest depth at which localised

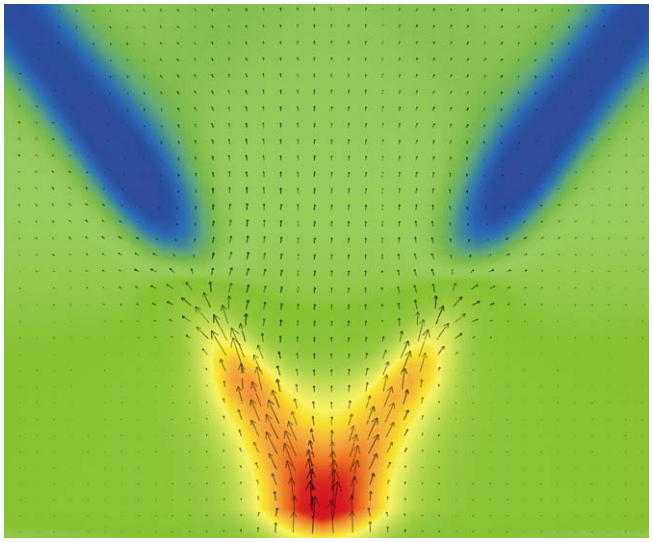

Fig. 12. Fluid flow vectors superimposed on contour plot of permeability ratio (red = permeability enhancement, blue = permeability reduction), Model A. Detail of bottom right corner, field of view ~3 × 3 km. Arrow length proportional to flux, maximum fluid flux = 2.15×10^{-8} $m^3/m^2/s$.

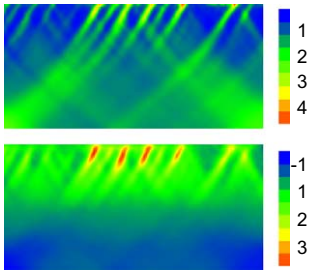

Fig. 13. Shear and volumetric strain rate ($s^{-1} \times 10^{-13}$, dilation positive), Model D.

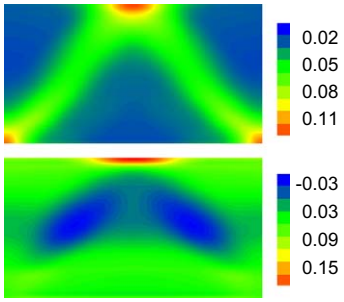

Fig. 14. Shear and volumetric strain after 5.5% shortening (dilation positive). Parameter values as for Model A, M increased to 1.1. Model width = 11.4 km.

permeability enhancement can take place is ~3.8 km. This brings into question genetic models for stratiform ore deposits, which invoke fluid focusing in faults as a mechanism for transporting fluids from depth to the surface through shallow, unconsolidated sediments (e.g. McGoldrick and Large, 1998). Our results imply that fluid focusing is not possible at depths shallower than ~3.8 km, although carbonates and fine-grained sediments may become cemented earlier than sandstones, and thus may allow development of permeable faults at shallower levels. Similarly, a steeper geothermal gradient would promote early cementation and hence allow permeability enhancement at shallower depths in sandstones (Fisher et al., 2003). The depth at which faults change from fluid pathways to seals is critical for the genesis of stratiform ore deposits, as this is the point at which fluids diverge out of the fault into the surrounding rock or sediment (Fig. 12).

Pore space created during brittle failure is reduced by a variety of sealing processes such as pressure solution and cementation, where the cement may be sourced locally from grain contact dissolution, or precipitated from externally-derived fluids moving through the fault (e.g. Robert et al., 1995; Parry, 1998; Renard et al., 2000; Sheldon and Ord, 2005). Fault sealing reduces permeability and may also increase the strength of the fault (Tenthorey et al., 2003); in Cam Clay terms this would be represented by expansion of the yield envelope, effectively preventing the fault rock from attaining critical state. Grain size reduction would enhance this strengthening effect. Our model considers the effect of initial grain size, but does not account for changes in grain size during deformation. Conversely, hydrothermal alteration of the wall rocks may create phyllitic mineral assemblages that weaken the fault (e.g. Bruhn et al., 1994).

The numerical models described in this paper represent a homogeneous, isotropic body of sediment that is rather different to natural sedimentary sequences. Layered sedimentary rocks tend to be anisotropic in their mechanical properties and permeability, and this anisotropy may be enhanced by shear strain hardening (Collins and Hilder, 2002), and by mineralogical or textural changes during shear failure. Faults themselves may also be anisotropic; for example, faults in porous sandstones commonly consist of a zone of compaction bands cut by a discrete (brittle) slip plane (Aydin and Johnson, 1983; Antonellini and Aydin, 1994), resulting in anisotropic permeability that inhibits flow across the fault, but allows flow in the plane of the fault. In the context of our model, this fault structure implies a slight change in loading path to allow the rock to switch from ductile to brittle behaviour. The required change in loading path may be very small, especially if the rock is at or close to critical state when the discrete slip plane is formed; local perturbations in the stress field due to heterogeneities in the rock may be sufficient to cause this change. However, our model cannot actually produce such structures, because strain hardening associated with compaction inhibits localisation in the ductile regime, hence compaction bands cannot form.

Table 3
Minimum depth for localised permeability increase in sandstone, based on porosity and P/P^* following initialisation

Deposition rate (m/Ma)	Geothermal gradient (°/km)	Grain radius (μm)	Minimum depth (m)
50	20	100	5280
50	20	200	5952
50	30	100	3805
50	30	200	4299
500	20	100	> 6000
500	20	200	> 6000
500	30	100	5280
500	30	200	5762

The effect of different loading paths on deformation style could have interesting consequences for faults in sedimentary basins undergoing inversion. Compressional loading paths are more likely to intersect the ductile, strain hardening section of the yield envelope, than extensional loading paths, especially if the porosity has previously been increased due to dilatant brittle failure in extension. Hence, dilatant faults formed in extension could become strain hardening, causing them to lock up during inversion. The situation may be complicated by erosional unloading associated with uplift, which can result in tensile stresses during inversion. Our model does not account for effects of erosion or deposition during deformation.

8. Evaluation of the method

The initial distributions of porosity and P/P^* versus depth predicted by our model are similar to those calculated by Fisher et al. (2003, in press), although their results show values at yield in an extensional regime, rather than the initial values following deposition in a uniaxial strain regime. The advantage of our method is that it permits investigation of the response of the system to different loading regimes following deposition, demonstrating the creation and destruction of porosity and permeability as a function of depth, burial history and stress regime. Nonetheless, the method of Fisher and coworkers remains a useful tool for making a quick evaluation of the likely failure mode and permeability evolution during deformation.

Numerical modelling has been used successfully in recent years to investigate coupling between deformation and fluid flow in the mid to upper crust (e.g. Ord and Henley, 1997; Ord and Oliver, 1997; Schaubs and Zhao, 2002; McLellan et al., 2004; Zhang et al., in press). These studies used the Mohr Coulomb constitutive model to simulate elasto-plastic behaviour. Mohr Coulomb is well-suited to modelling deformation of low porosity rocks in the brittle regime, but it lacks the porosity-dependent yield behaviour of the Cam Clay model and hence is not appropriate for simulating deformation of high porosity rocks. Strain hardening/softening is not an intrinsic component of the Mohr Coulomb model, although it can be imposed by varying rock properties as a function of shear and/or volumetric strain (Ord, 1991). Localisation in a Mohr Coulomb material is a consequence of non-associated plasticity and/or of corners on the yield surface (Rudnicki and Rice, 1975; Vermeer and de Borst, 1984), and of strain softening if this is imposed on the model. This contrasts with the

Cam Clay model described in this paper, in which the flow rule is associated, the yield surface is smooth, and localisation is a consequence of intrinsic strain softening in the dilatant, brittle regime.

The assumption of associated plasticity, with the transition from dilation to compaction occurring at the peak of the yield envelope, is probably the most significant limitation of our model for deformation of porous sandstones. Data presented by Wong et al. (1997) suggest that the transition from dilation to compaction occurs at $P/P^* \sim 0.25$, well before the peak of the yield envelope, but the associated flow rule forces the transition to coincide with the peak of the yield envelope, which is consistently in the range $0.45 < P/P^* < 0.55$. Consequently, our model tends to over-estimate dilatancy and under-estimate compaction. Compaction bands are a common feature of deformed sandstones (e.g. Aydin and Johnson, 1983; Antonellini and Aydin, 1994; Olsson, 1999) which are not predicted by the Cam Clay model because strain hardening inhibits localisation. Formation of compaction bands implies a flow rule that permits localisation in the strain hardening regime (Issen and Rudnicki, 2000; Olsson and Holcomb, 2000; Borja and Aydin, 2004; Challa and Issen, 2004; Rudnicki, 2004). Further analysis of experimental data, particularly that which records the post-yield evolution of P, Q and ϕ (e.g. Wong et al., 1992), would be required in order to constrain the flow rule more precisely.

The faults or shear zones that develop in our models tend to fail continuously until the loading conditions are changed. This behaviour contrasts with that of real faults in the brittle regime, which typically undergo discrete slip events interspersed with periods of quiescence. The continuous failure mode displayed by our models represents the time-averaged effect of multiple, discrete slip events. Our models cannot reproduce the transient fluid flow patterns associated with discrete slip events, which play an important role in mineralisation and the earthquake cycle (e.g. Sibson, 2001; Sheldon and Ord, 2005).

Our models were deformed at a longitudinal strain rate of $\sim 10^{-13}\ s^{-1}$, which is at the upper end of typical geological strain rates (e.g. Pfiffner and Ramsay, 1982). As mentioned earlier, this relatively high strain rate is necessitated by the explicit calculation method used in FLAC3D. The effect of a high strain rate is to alter the feedback between deformation and fluid flow, as the fluid has less time to respond to changes in fluid pressure induced by volumetric strain. Hence, fluid pressure will tend to be higher in compacting regions and lower in dilating regions than would be expected at a lower strain rate. This may result in steeper fluid pressure gradients and higher flow rates. It also affects the mechanical behaviour, as high fluid pressure decreases the effective stress, and vice versa. This effect may speed up the approach to critical state; shear-enhanced compaction will result in increased fluid pressure, which decreases the mean effective stress and thus moves the rock closer to the peak of the yield envelope, whereas dilatant brittle failure results in decreased fluid pressure and increased effective stress, again moving the rock closer to the peak of the yield envelope.

Running simulations at a high strain rate would be more problematic if the constitutive model included time-dependence as well as elasto-plasticity. Time-dependence reflects diffusive deformation mechanisms such as pressure solution, and the development of ‘‘damage’’ or microcracks prior to macroscopic failure. This aspect of porous rock behaviour appears to be captured by the damage mechanics formulation of Hamiel et al. (2004), in which the strength and elastic moduli of the rock depend on the density of microcracks in a representative volume of rock. Future developments in this field may resolve some of the limitations with the Cam Clay model.

9. Conclusions and future directions

Previous studies have identified commonality between the behaviour of porous rocks and that of soils, which is embodied in the concepts of CSSM. This study has used results of deformation experiments to parameterise a CSSM model for sandstones, and implemented this behaviour in a numerical model to create a tool for investigating deformation and fluid flow in sedimentary basins. The numerical model validates and expands on concepts described by Fisher et al. (2003, in press), demonstrating the effect of varying grain size, geothermal gradient and deposition rate on the behaviour of sandstones in compressional and extensional regimes. Our model permits exploration of the effects of different loading regimes on deformation and fluid flow within sedimentary basins. Permeability changes due to deformation are shown to have a profound impact on fluid flow, with fluid being focused through dilatant, brittle faults at depths where host rock porosity is low enough to allow permeability enhancement, while faults at higher levels act as barriers to fluid flow. The depth of transition from permeability reduction to permeability enhancement depends on geothermal gradient, grain size and burial history, being deeper in areas of low geothermal gradient, fast deposition and coarse grain size.

The purpose of this paper was to describe the parameterisation of a CSSM model for sandstones, and to illustrate its implementation in a numerical code by way of simple, plane strain examples. The FLAC3D code is capable of fully three-dimensional simulations, the only constraint being the time taken to run 3D models (days rather than hours). Areas for future work include parameterisation of the model for other rock types, such as shale and limestone, and investigation into the behaviour of layered sequences in which each layer has different mechanical properties. Basin inversion could be investigated by switching from extension to compression at some point during a model run; it would be interesting to observe the behaviour in compression of regions that had previously been hardened or softened during yield in extension. Reactivation of basement faults and consequent effects on the overlying sedimentary sequence could be investigated by adding a strong, brittle layer to the base of the model with a pre-defined plane of weakness representing an earlier fault. The effect of temperature on fluid flow should also be considered; an interesting avenue of research would be to consider the effect of relatively impermeable faults on convection patterns in sedimentary basins, c.f. previous studies of convection in which faults were assumed to be significantly more

permeable than their host rocks all the way to the surface, e.g. Garven et al. (2001).

A longer-term goal is to identify a modelling approach that resolves the limitations of the present model, especially the assumption of associated plasticity, and the lack of time-dependence in the mechanical behaviour. The damage mechanics formulations of Hamiel et al. (2004) and Ricard and Bercovici (2003) go some way towards achieving this aim, and may also lead to a more self-consistent formulation for permeability evolution than the empirical approach taken here. Challenges lie ahead in terms of understanding how to parameterise the damage mechanics formulation, in particular whether existing experimental results can be used, or whether new experiments are required. In the meantime, our modified version of Cam Clay in FLAC3D provides a useful tool for simulating deformation and fluid flow in porous rocks, with a wide range of potential applications in the fields of hydrocarbon and mineral exploration.

Acknowledgements

Work reported here was conducted as part of the Predictive Mineral Discovery Cooperative Research Centre. This paper is published with the permission of the CEO, pmd*CRC and the CEO, Geoscience Australia. Quentin Fisher and Teng-Fong Wong are thanked for their constructive reviews. HAS thanks colleagues at CSIRO and GA for stimulating discussions.

References

Antonellini, M., Aydin, A., 1994. Effect of faulting on fluid flow in porous sandstones: petrophysical properties. Bulletin of the American Association of Petroleum Geologists 78, 355–377.

Atkinson, J.H., Bransby, P.L., 1978. The Mechanics of Soils: An Introduction to Critical State Soil Mechanics. McGraw-Hill, London.

Aydin, A., Johnson, A.M., 1983. Analysis of faulting in porous sandstones. Journal of Structural Geology 5, 19–31.

Baud, P., Schubnel, A., Wong, T.F., 2000. Dilatancy, compaction, and failure mode in Solnhofen limestone. Journal of Geophysical Research 105, 19289–19303.

Bernabé, Y., Fryer, D.T., Shively, R.M., 1994. Experimental observations of the elastic and inelastic behavior of porous sandstones. Geophysical Journal International 117, 403–418.

Bethke, C.M., 1985. A numerical model of compaction-driven groundwater flow and heat transfer and its application to the paleohydrology of intracratonic sedimentary basins. Journal of Geophysical Research 90, 6817–6828.

Bigoni, D., Piccolroaz, A., 2004. Yield criteria for quasibrittle and frictional materials. International Journal of Solids and Structures 41, 2855–2878.

Borja, R.I., Aydin, A., 2004. Computational modeling of deformation bands in granular media. I. Geological and mathematical framework. Computer Methods in Applied Mechanics and Engineering 193, 2667–2698.

Brown, E.T., Yu, H.S., 1988. A model for the ductile yield of porous rock. International Journal for Numerical and Analytical Methods in Geomechanics 12, 679–688.

Bruhn, R.L., Parry, W.T., Yonkee, W.A., Thompson, T., 1994. Fracturing and hydrothermal alteration in normal-fault zones. Pure and Applied Geophysics 142, 609–644.

Celle, C.C., Cheatham, J.B., 1981. Anisotropic hardening of an initially isotropic porous limestone. Rock Mechanics 13, 221–233.

Challa, V., Issen, K.A., 2004. Conditions for compaction band formation in porous rock using a two-yield surface model. Journal of Engineering Mechanics – ASCE 130, 1089–1097.

Collin, F., Cui, Y.J., Schroeder, C., Charlier, R., 2002. Mechanical behaviour of Lixhe chalk partly saturated by oil and water: experiment and modelling. International Journal for Numerical and Analytical Methods in Geomechanics 26, 897–924.

Collins, I.F., Hilder, T., 2002. A theoretical framework for constructing elastic/plastic constitutive models of triaxial tests. International Journal for Numerical and Analytical Methods in Geomechanics 26, 1313–1347.

Collins, I.F., 2003. A systematic procedure for constructing critical state models in three dimensions. International Journal of Solids and Structures 40, 4379–4397.

Cundall, P.A., Board, M., 1988. A microcomputer program for modelling large-strain plasticity problems. In: Swoboda, C. (Ed.), Numerical Methods in Geomechanics. Proceedings of the Sixth International Conference on Numerical Methods in Geomechanics. Balkema, Rotterdam, pp. 2101–2108.

Cuss, R.J., Rutter, E.H., Holloway, R.F., 2003. The application of critical state soil mechanics to the mechanical behaviour of porous sandstones. International Journal of Rock Mechanics and Mining Sciences 40, 847–862.

David, C., Menendez, B., Zhu, W., Wong, T.F., 2001. Mechanical compaction, microstructures and permeability evolution in sandstones. Physics and Chemistry of the Earth, Part A: Solid Earth and Geodesy 26, 45–51.

Drucker, D.C., 1951. A more fundamental approach to plastic stress strain relations. In: Proceedings of the First U.S. National Congress on Applied Mechanics, pp. 487–491.

Ehrenburg, S.N., 1990. Relationship between diagenesis and reservoir quality in sandstones of the Garn formation, Haltenbanken, mid-Norwegian continental shelf. Bulletin of the American Association of Petroleum Geologists 74, 1538–1558.

Elliott, G.M., Brown, E.T., 1985. Yield of a soft, high porosity rock. Geotechnique 35, 413–422.

Elliott, G.M., Brown, E.T., 1986. Further development of a plasticity approach to yield in porous rock. International Journal of Rock Mechanics and Mining Sciences and Geomechanics Abstracts 23, 151–156.

Fisher, Q.J., Casey, M., Harris, S.D., Knipe, R.J., 2003. Fluid-flow properties of faults in sandstone: the importance of temperature history. Geology 31, 965–968.

Fisher, Q.J., Harris, S.D., Casey, M., Knipe, R.J. Influence of grain-size and geothermal gradient on the ductile-to-brittle transition in arenaceous sedimentary rocks: implications for fault structure and fluid flow. In: Lewis, H. and Couples, G.D. (Eds.), Damage and localisation. Geological Society of London Special Publication, in press.

Fisher, Q.J., Knipe, R.J., 1998. Fault sealing processes in siliciclastic sediments. In: Jones, G., Fisher, Q.J., Knipe, R.J. (Eds.), Faulting, Fault Sealing and Fluid Flow in Hydrocarbon Reservoirs. Geological Society of London Special Publication 147, 117–134 (Geological Society of London, London).

Fisher, Q.J., Knipe, R.J., 2001. The permeability of faults within siliciclastic petroleum reservoirs of the North Sea and Norwegian continental shelf. Marine and Petroleum Geology 18, 1063–1081.

Garven, G., Bull, S.W., Large, R.R., 2001. Hydrothermal fluid flow models of stratiform ore genesis in the McArthur Basin, Northern Territory, Australia. Geofluids 1, 289–311.

Gerogiannopoulos, N.G., Brown, E.T., 1978. The critical state concept applied to rock. International Journal of Rock Mechanics and Mining Sciences and Geomechanics Abstracts 15, 1–10.

Graham, J., Noonan, M.L., Lew, K.V., 1983. Yield states and stress–strain relationships in a natural plastic clay. Canadian Geotechnical Journal 20, 502–516.

Hamiel, Y., Lyakhovsky, V., Agnon, A., 2004. Coupled evolution of damage and porosity in poroelastic media: theory and applications to deformation of porous rocks. Geophysical Journal International 156, 701–713.

Harrison, W.J., Summa, L.L., 1991. Paleohydrology of the Gulf of Mexico basin. American Journal of Science 291, 109–176.

Hobbs, B.E., Mühlhaus, H.B., Ord, A., 1990. Instability, softening and localization of deformation. In: Knipe, R.J., Rutter, E.H. (Eds.),

Deformation mechanisms, rheology and tectonics. Geological Society of London Special Publications 54, 143–165 (Geological Society of London, London).

Homand, S., Shao, J.F., 2000. Mechanical behaviour of a porous chalk and effect of saturating fluid. Mechanics of Cohesive-frictional Materials 5, 583–606.

Issen, K.A., Rudnicki, J.W., 2000. Conditions for compaction bands in porous rock. Journal of Geophysical Research 105, 21529–21536.

Itasca Consulting Group, 2002. FLAC3D: Fast Lagrangian Analysis of Continua in 3 dimensions. Itasca, Minneapolis.

Khan, A.S., Xiang, Y., Huang, S.J., 1991. Behavior of Berea sandstone under confining pressure Part 1: yield and failure surfaces, and nonlinear elastic response. International Journal of Plasticity 7, 607–624.

Kieffer, B., Schott, J., Oelkers, E.H., Schott, J., 1999. An experimental study of the reactive surface area of the Fontainebleau sandstone as a function of porosity, permeability and fluid flow rate. Geochimica et Cosmochimica Acta 63, 3525–3534.

Knipe, R.J., 1992. Faulting processes and fault seal. In: Larsen, R.M., Brekke, H., Larsen, B.T., Talleraas, E. (Eds.), Norwegian Petroleum Society Special Publication 1. Elsevier, New York, pp. 325–342.

Knipe, R.J., 1993. The influence of fault zone processes and diagenesis on fluid flow. In: Horbury, A.D., Robinson, A.G. (Eds.), Diagenesis and Basin Development. AAPG Studies in Geology, vol. 36. AAPG, Tulsa, OK, pp. 135–154.

Ling, H.I., Yue, D., Kaliakin, V.N., Themelis, N.J., 2002. Anisotropic elastoplastic bounding surface model for cohesive soils. Journal of Engineering Mechanics 128, 748–758.

Lubarda, V.A., Mastilovic, S., Knap, J., 1996. Brittle–ductile transition in porous rocks by cap model. Journal of Engineering Mechanics-ASCE 122, 633–642.

McGoldrick, P., Large, R., 1998. Proterozoic stratiform sediment-hosted Zn–Pb–Ag deposits. AGSO Journal of Australian Geology and Geophysics 17, 189–196.

McLellan, J.G., Oliver, N.H.S., Schaubs, P.M., 2004. Fluid flow in extensional environments; Numerical modelling with an application to Hamersley iron ores. Journal of Structural Geology 26, 1157–1171.

Menéndez, B., Zhu, W.L., Wong, T.F., 1996. Micromechanics of brittle faulting and cataclastic flow in Berea sandstone. Journal of Structural Geology 18, 1–16.

Morris, J.P., Lomov, I.N., Glenn, L.A., 2003. A constitutive model for stress-induced permeability and porosity evolution of Berea sandstone. Journal of Geophysical Research 108, 2485, doi:10.1029/2001JB000463.

Oelkers, E.H., 1996. Physical and chemical properties of rocks and fluids for chemical mass transport calculations. In: Lichtner, P.C., Steefel, C.I., Oelkers, E.H. (Eds.), Reactive Transport in Porous Media. Reviews in Mineralogy, vol. 34. Mineralogical Society of America, Washington, pp. 131–192.

Olsson, W.A., 1999. Theoretical and experimental investigation of compaction bands. Journal of Geophysical Research 104, 7219–7228.

Olsson, W.A., Holcomb, D.J., 2000. Compaction localization in porous rock. Geophysical Research Letters 27, 3537–3540.

Ord, A., 1991. Deformation of rock – a pressure-sensitive, dilatant material. Pure and Applied Geophysics 137, 337–366.

Ord, A., Henley, S., 1997. Fluid pumping: Some exploratory numerical methods. Physics and Chemistry of the Earth, Part A: Solid Earth and Geodesy 22, 49–56.

Ord, A., Oliver, N.H.S., 1997. Mechanical controls on fluid flow during regional metamorphism: some numerical models. Journal of Metamorphic Geology 15, 345–359.

Parry, W.T., 1998. Fault-fluid compositions from fluid-inclusion observations and solubilities of fracture-sealing minerals. Tectonophysics 290, 1–26.

Paterson, M.S., Wong, T.F., 2005. Experimental Rock Deformation – The Brittle Field. Springer.

Pfiffner, O.A., Ramsay, J.G., 1982. Constraints on geological strain rates: Arguments from finite strain states of naturally deformed rocks. Journal of Geophysical Research 87, 311–321.

Renard, F., Gratier, J.P., Jamtveit, B., 2000. Kinetics of crack-sealing, intergranular pressure solution, and compaction around active faults. Journal of Structural Geology 22, 1395–1407.

Ricard, Y., Bercovici, D., 2003. Two-phase damage theory and crustal rock failure: the theoretical 'void' limit, and the prediction of experimental data. Geophysical Journal International 155, 1057–1064.

Robert, F., Boullier, A.M., Firdaous, K., 1995. Gold-quartz veins in metamorphic terranes and their bearing on the role of fluids in faulting. Journal of Geophysical Research 100, 12861–12879.

Roscoe, K.H., Burland, J.B., 1968. On the generalised stress–strain behavior of 'wet clay'. In: Heyman, J., Leckie, F.A. (Eds.), Engineering Plasticity. Cambridge University Press, Cambridge, pp. 535–609.

Rudnicki, J.W., 2004. Shear and compaction band formation on an elliptic yield cap. Journal of Geophysical Research 109 (Article No. B03402).

Rudnicki, J.W., Rice, J.R., 1975. Conditions for the localization of deformation in pressure-sensitive dilatant materials. Journal of the Mechanics and Physics of Solids 3, 209–214.

Rutter, E.H., Hadizadeh, J., 1991. On the influence of porosity on the low-temperature brittle–ductile transition in siliciclastic rocks. Journal of Structural Geology 13, 609–614.

Schaubs, P.M., Zhao, C., 2002. Numerical models of gold-deposit formation in the Bendigoz–Ballarat Zone, Victoria. Australian Journal of Earth Sciences 49, 1077–1096.

Schofield, A., Wroth, P., 1968. Critical State Soil Mechanics. McGraw-Hill, London.

Scott, T.E., Nielson, K.C., 1991. The effects of porosity on the brittle–ductile transition in sandstones. Journal of Geophysical Research 96, 405–414.

Sheldon, H.A., Ord, A., 2005. Evolution of porosity, permeability and fluid pressure in dilatant faults post-failure: Implications for fluid flow and mineralization. Geofluids 5, 272–288.

Sibson, R.H., 2001. Seismogenic framework for hydrothermal transport and ore deposition. Reviews in Economic Geology 14, 25–50.

Steiger, R.P., Leung, P.K., 1991. Critical state shale mechanics. In: Roegiers, J.C. (Ed.), Rock Mechanics As a Multidisciplinary Science. Proceedings – Symposium on Rock Mechanics 32. Balkema, Rotterdam, pp. 293–302.

Tenthorey, E., Cox, S.F., Todd, H.F., 2003. Evolution of strength recovery and permeability during fluid-rock reaction in experimental fault zones. Earth and Planetary Science Letters 206, 161–172.

Thompson, A.B., 1997. Flow and focusing of metamorphic fluids. In: Jamtveit, B., Yardley, B.W.D. (Eds.), Fluid Flow and Transport in Rocks. Chapman and Hall, London, pp. 297–314.

Vajdova, V., Baud, P., Wong, T.F., 2004. Compaction, dilatancy, and failure in porous carbonate rocks. Journal of Geophysical Research 109 (Article no. B05204).

Vermeer, P.A., de Borst, R., 1984. Non-associated plasticity for soils, concrete and rock. Heron 29, 1–62.

Walderhaug, O., 1996. Kinetic modeling of quartz cementation and porosity loss in deeply buried sandstone reservoirs. Bulletin of the American Association of Petroleum Geologists 80, 731–745.

Wong, T.F., David, C., Zhu, W.L., 1997. The transition from brittle faulting to cataclastic flow in porous sandstones: mechanical deformation. Journal of Geophysical Research 102, 3009–3025.

Wong, T.F., Szeto, H., Zhang, J., 1992. Effect of loading path and porosity on the failure mode of porous rocks. Applied Mechanics Reviews 45, 281–293.

Wood, D.M., 1990. Soil Behaviour and Critical State Soil Mechanics. Cambridge University Press, Cambridge.

Zhang, J.X., Wong, T.F., Davis, D.M., 1990. Micromechanics of pressure-induced grain crushing in porous rocks. Journal of Geophysical Research and Planets 95, 341–352.

Zhang, Y., Sorjonen-Ward, P., Ord, A., Southgate, P.N. Fluid flow during deformation associated with structural closure of the Isa superbasin at 1575 ma in the central and northern Lawn Hill Platform, northern Australia. Economic Geology, in press.

Zhu, W.L., Montesi, L.G.J., Wong, T.F., 1997. Shear-enhanced compaction and permeability reduction: triaxial extension tests on porous sandstone. Mechanics of Materials 25, 199–214.

Zhu, W.L., Wong, T.F., 1997. The transition from brittle faulting to cataclastic flow: permeability evolution. Journal of Geophysical Research 102, 3027–3041.

Zhu, W.L., Wong, T.F., 1999. Network modeling of the evolution of permeability and dilatancy in compact rock. Journal of Geophysical Research 104, 2963–2971.